

Dynamics of the Local Structure

Chapter Outline

7.1. Measurement of Inelastic Scattering	297	7.4. Dynamic Pair-Density Function	310
7.1.1. Neutron Triple-Axis-Spectrometer	298	7.5. Effect of Inelastic Scattering on the PDF	314
7.1.2. IXS Measurement	299	7.5.1. Placzek Correction	314
7.1.3. Chopper Spectrometer	301	7.5.2. Effective Energy Window for the Neutron PDF Method	319
7.2. Dynamic Structure Factor	303	7.5.3. Phonon Dispersion and the PDF	319
7.2.1. Single-Phonon Scattering	303	7.5.4. Hybrid Techniques	320
7.2.2. Multi-Phonon Process	306	A7.1. Simple Derivation	322
7.3. Correlated Dynamics and the PDF	308		

7.1. MEASUREMENT OF INELASTIC SCATTERING

In the discussion so far, we assumed that the instrument of measurement has poor energy resolution and measures the intensity integrated over all the energy transfers. It is possible, however, to set up equipment in a way that the energy lost or gained during the scattering can be measured. Such an experiment, an inelastic scattering measurement, is particularly straightforward for neutron scattering, since the energy of neutrons used in the measurement (10 meV to 1 eV) is comparable to the energy of excitations in the solids, such as lattice dynamics. An inelastic X-ray scattering (IXS) measurement is more difficult, since the incident X-ray energy is of the order of 10–100 keV, much larger than the energy scale of interest. It became feasible only recently with the advent of third-generation synchrotron sources and

advances in monochromator technology. However, it is a very promising method to determine the dynamics of electrons and atoms.

In this chapter, we describe how to carry out an inelastic scattering measurement and how the motion of atoms will affect the scattered intensity of neutrons and X-rays, introduce the concept of the dynamic PDF, and discuss how the lattice dynamics affect the neutron PDF. Magnetic excitations are outside the scope of this chapter, but the discussions on phonons can be readily extended into the treatments of magnons and crystal-field excitations. The pulsed neutron scattering measurements to determine the PDF, described in [Chapters 4](#) and [5](#), are in-between pure elastic and inelastic measurements and this introduces complications as well as opportunities. The PDF determined by a regular powder neutron scattering measurement includes both elastic and inelastic scattering intensities; however, the special geometry of the measurement means that it captures part of the dynamics while ignoring the rest. Local lattice dynamics of a certain range of energy transfers result in irregular distortions of the PDF that depend upon the detector angle.

7.1.1. Neutron Triple-Axis-Spectrometer

For a steady-state neutron or X-ray source, a triple-axis spectrometer offers the capacity of measuring the inelastic scattering intensity (for details see [Tranquada *et al.*, 2002](#)). A triple-axis spectrometer ([Fig. 7.1](#)) consists of a monochromator, sample, and analyzer, each placed on a separate goniometer to allow the orientation of each to be independently controlled by a motor. Thus, one can specify the energy and direction of the incident beam, the sample orientation, and the energy and direction of the detected scattered beam.

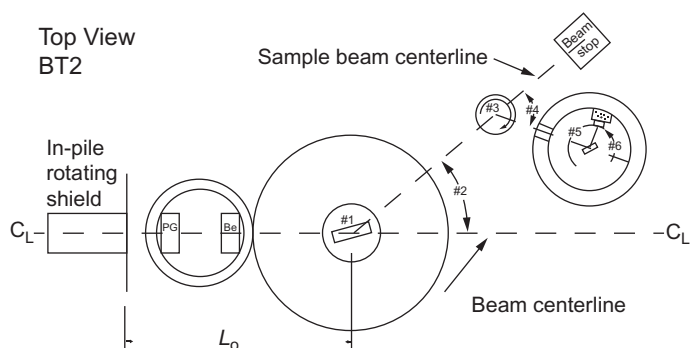


FIGURE 7.1 Schematic of a triple-axis spectrometer (actually BT2 at the National Center for Neutron Research at NIST in Maryland, USA) used in inelastic neutron scattering measurement with a reactor source. The three axes are the monochromator (#1), the sample (#3), and the analyzer crystal. (#5). This spectrometer also has pyrolytic graphite (PG) and beryllium filters upstream of the monochromator. The monochromator and analyzers are either PG or Heusler alloy for unpolarized and polarized neutron experiments, respectively.

The scattering process is then determined by the energy and momentum transfers,

$$\hbar\omega = \hbar\omega_{\text{init}} - \hbar\omega_{\text{final}} \quad (7.1)$$

and

$$\mathbf{Q} = \mathbf{k}_{\text{init}} - \mathbf{k}_{\text{final}}, \quad (7.2)$$

where an incoming neutron or X-ray photon has the energy $\hbar\omega_{\text{init}}$ and the momentum \mathbf{k}_{init} and is scattered into the state with the energy $\hbar\omega_{\text{final}}$ and the momentum $\mathbf{k}_{\text{final}}$. Thus for neutrons,

$$\hbar\omega = \frac{\hbar^2}{2m} (k_{\text{init}}^2 - k_{\text{final}}^2), \quad (7.3)$$

where m is the neutron mass, $k_{\text{final}} = |\mathbf{k}_{\text{final}}|$, $k_{\text{init}} = |\mathbf{k}_{\text{init}}|$ and for X-rays,

$$\hbar\omega = \hbar c (k_{\text{init}} - k_{\text{final}}), \quad (7.4)$$

where c is the speed of light. For both cases,

$$Q^2 = k_{\text{final}}^2 + k_{\text{init}}^2 - 2k_{\text{final}}k_{\text{init}} \cos 2\theta, \quad (7.5)$$

where 2θ is the angle between \mathbf{k}_{init} and $\mathbf{k}_{\text{final}}$. For an elastic scattering ($\omega = 0$, $k = k_{\text{init}} = k_{\text{final}}$) process,

$$Q_0 = 2k \sin \theta = \frac{4\pi \sin \theta}{\lambda}. \quad (7.6)$$

However, for an inelastic process, Q is different from Q_0 . The energy and momentum lost by the probe particle are transferred to the solid. Thus, the energy gained by the solid is $\hbar\omega$. This transferred energy and momentum can create or annihilate (with negative energy transfer) excitations such as lattice vibrations (phonons) or spin waves (magnons).

7.1.2. IXS Measurement

The measurement of phonons with X-rays is much more difficult since the energy transfer is smaller than the X-ray energy by many orders of magnitude. For instance, if one uses an X-ray of 10 keV and tries to measure a phonon with the energy of 10 meV, an energy resolution of at least 10^{-7} is required. Only recently such a measurement became feasible because of advances in synchrotron sources and crystal monochromators. As we discuss later, progress is rapid, especially by way of decreasing data collection times, opening the door to qualitatively different experiments such as parametric studies, as a function of temperature for example, studies of phase diagrams, and so on. So far, most of the inelastic scattering measurements of phonons have been carried out with neutrons, but this is changing. On the other hand,

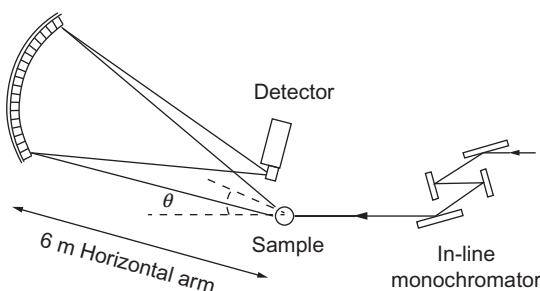


FIGURE 7.2 Schematic of the inelastic X-ray scattering spectrometer system, 3ID-C of the APS, Argonne National Laboratory (Sinn *et al.*, 2001).

measurements of electronic excitations, such as the Compton scattering and interband transitions, do not require such high resolution. While these measurements are not easy because of low scattering intensity, IXS measurements of electronic process are becoming an important research technique. Unlike X-ray absorption spectroscopy, it provides momentum resolved information, making it easier to make connection with the calculated band structure.

An example of the schematic plan of an IXS station is given in Fig. 7.2. In order to achieve such a high-energy resolution, backscattering geometry is used for the monochromator and analyzer. In addition, the monochromator and analyzer have to be thermally and mechanically well isolated so that they are extremely stable with respect to temperature and vibration. At the ESRF, the energy scan is accomplished by changing the temperature, and therefore the d -spacing due to thermal expansion, of the analyzer crystal!

While neutrons track the dynamics of nuclei, X-rays bring out information on electron dynamics. While the dynamics of electrons tightly bound to the nuclei, the core electrons, simply follow the lattice dynamics, the dynamics of valence electrons provide direct information on the electronic band structure of the solid. For the determination of the phonon dispersion, neutron scattering is a better choice most of the time. But as it is much easier to focus an X-ray beam than a neutron beam, IXS can be used in determining the phonon dispersion of very small crystals or even thin films and surfaces. For determining the dynamics of valence electrons in the bulk, IXS is a unique method. The method of angle-resolved photoemission spectroscopy, though powerful, suffers from electron life-time and surface effects (because the escape depth of photoelectrons is only a few nanometers) making the results difficult to interpret. IXS, on the other hand, is a cleaner method to probe the bulk, without the complication of the final-state interaction. It should become a powerful method to determine directly, not only the single particle electron dispersion, but also the electron–phonon coupling.

7.1.3. Chopper Spectrometer

For a pulsed neutron source, a chopper is used instead of a crystal monochromator to produce a monochromatic beam. A chopper is a cylinder with a narrow path that rotates at high speed. It allows neutrons within a certain energy range to pass through and plays the role of a low resolution monochromator. The incident energy is chosen by adjusting the timing of the opening of the chopper with respect to the generation of the pulse of neutrons. The energy band-pass is set by changing the speed of rotation. The energy of the scattered neutron is determined by the time-of-flight method using a large array of detectors placed around the sample (Fig. 7.3). The reverse of this method is to fix the energy of the scattered neutrons by using an array of filters or analyzer crystals placed between the sample and the detectors in the backscattering geometry, as used on the IRIS spectrometer at ISIS. Much higher resolution, though a narrower range of energy transfers, is attained by this method. This type of spectrometer is illustrated in Fig. 7.4.

For a fixed incident energy, Eqs. (7.3) and (7.5) yield,

$$Q^2 = 2k_{\text{init}}^2 \left[1 - \frac{m\omega}{\hbar k_{\text{init}}^2} - \cos(2\theta) \left(1 - \frac{2m\omega}{\hbar k_{\text{init}}^2} \right)^{1/2} \right]. \quad (7.7)$$

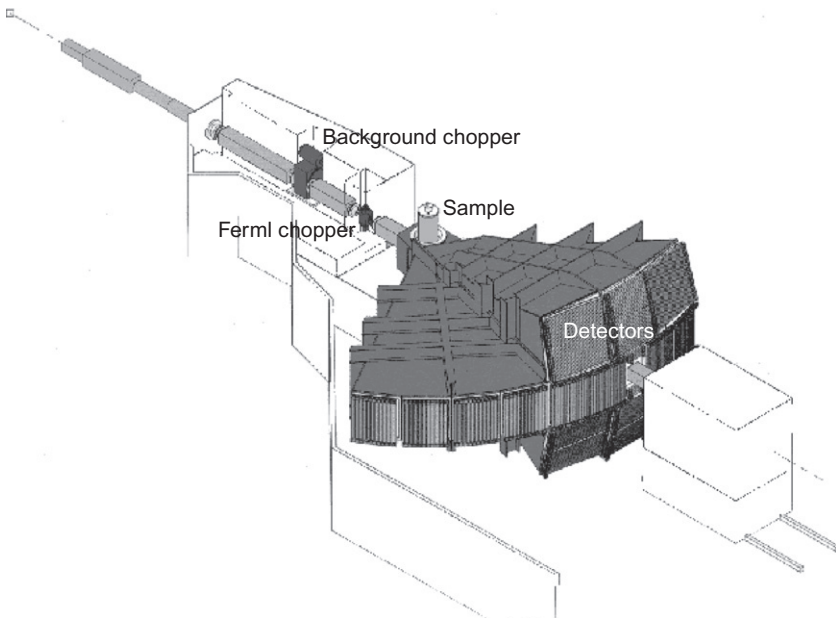


FIGURE 7.3 Chopper spectrometer (MAPS) used in inelastic neutron scattering measurement with a pulsed neutron source.

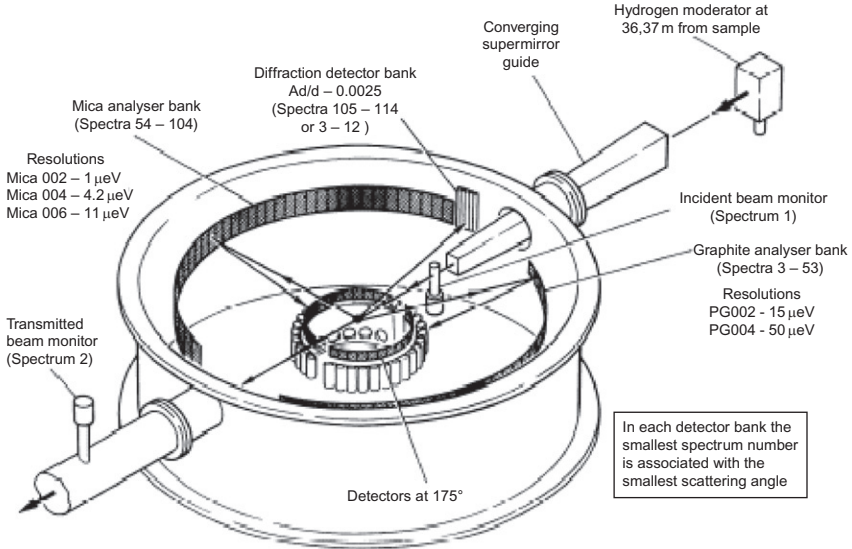


FIGURE 7.4 Backscattering spectrometer IRIS at ISIS. This configuration provides higher resolution but a narrower range of energy transfers can be accessed compared with chopper spectrometers such as MAPS.

For each detector placed at an angle 2θ , the TOF spectrum produces the values of the dynamic structure factor, $S(Q, \omega)$ along the Q - ω curve determined by Eq. (7.7). $S(Q, \omega)$ is related to the double-differential scattering cross section introduced in Chapter 5 according to

$$\frac{d^2\sigma}{d\Omega dE_s} = \left(\frac{k_{\text{final}}}{k_{\text{init}}} \right) [\sigma_{\text{coh}} S_{\text{coh}}(Q, \omega) + \sigma_{\text{inc}} S_{\text{inc}}(Q, \omega)], \quad (7.8)$$

where σ is the scattering cross section and “coh” and “inc” refer to the coherent and incoherent scattering, respectively. By assembling the data from various detectors placed all around the sample, the entire $S(Q, \omega)$ map can be obtained. For example, $S(Q, \omega)$ from the MAPS spectrometer of ISIS is shown in Fig. 7.5. Note that for a given Q , the maximum in ω is obtained for $2\theta = \pi$ (backscattering). For this case, the Q - ω relation is a simple parabola:

$$\omega = \frac{\hbar}{2m} Q(2k_{\text{init}} - Q) \quad (7.9)$$

$S(Q, \omega)$ can be determined only within this parabola. In particular, for small Q ,

$$\omega \leq \frac{\hbar k_{\text{init}}}{m} Q = v_{\text{init}} Q, \quad (7.10)$$

where v_{init} is the velocity of the incident neutron beam. Thus, in order to measure excitations with small Q and large ω , the use of neutrons with high initial velocity, thus high-incident energy, is required. While it is impossible to set $2\theta = \pi$ because the detection system shadows the incoming beam, if 2θ is close to π , $\cos(2\theta)$ is practically unity, justifying the use of Eq. (7.9).

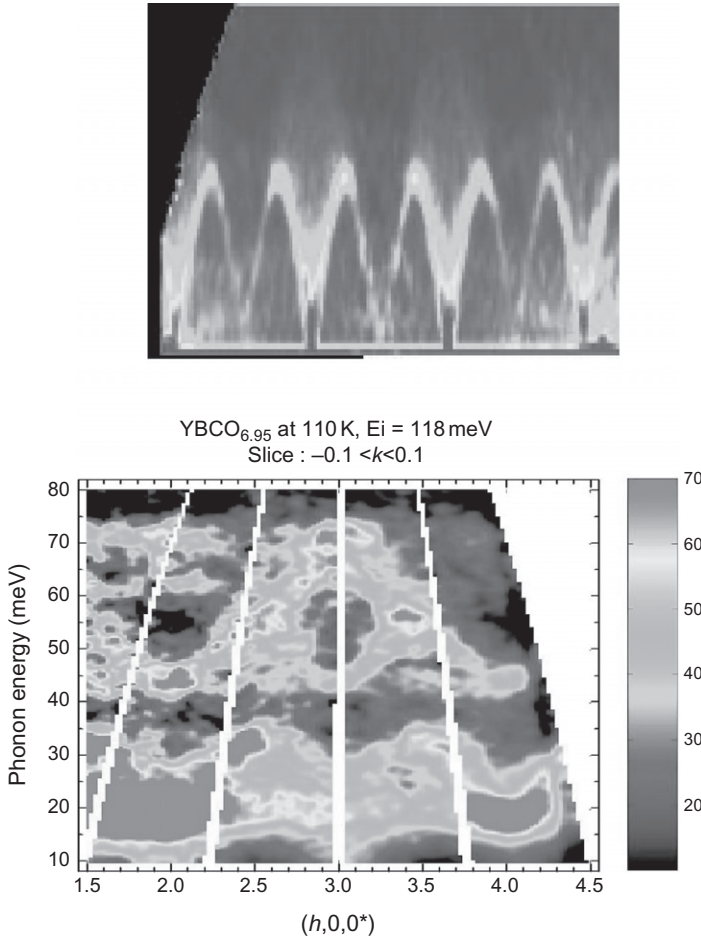


FIGURE 7.5 $S(Q, \omega)$ functions determined using the MAPS chopper spectrometers at ISIS. (a) Spin wave dispersion curves (magnetic excitations) from a quasi-1D quantum magnetic system, KCuF₃ (Lake *et al.*, 2000). (b) Phonon dispersion map of YBa₂Cu₃O_{6.95}. In both cases, the vertical axis is energy transfer, ω , and the horizontal axis is momentum transfer, Q . The color scale indicates intensity, red being high and blue/black low. The dispersion curves of the excitations are directly evident in the raw data as regions of high intensity at well-defined positions of energy and momentum (Egami *et al.*, 2002).

7.2. DYNAMIC STRUCTURE FACTOR

7.2.1. Single-Phonon Scattering

The intensity of particles inelastically scattered by phonons is described by the phonon dynamic structure factor,

$$S(\mathbf{Q}, \omega) = \frac{1}{N \langle b \rangle^2} \sum_{\nu, \mu} b_{\nu} b_{\mu} \int \langle \langle e^{i\mathbf{Q} \cdot (\mathbf{R}_{\nu}(0) - \mathbf{R}_{\mu}(t))} \rangle \rangle e^{-i\omega t} dt, \quad (7.11)$$

where $\langle\langle \dots \rangle\rangle$ represents an ensemble average. This expression is similar to Eq. (2.9), but is time dependent. More detailed treatments are given, for instance, in Lovesey (1984). To derive this equation, we go back to Chapter 2 and derive the phase factor again (Appendix 2.1), but including the time dependence explicitly. Such a derivation is given in Appendix A7.1.

To derive equations for the dynamics of particles, it is useful to be able to switch between the time and frequency domains. This is done by a Fourier-transform where we define the scattering function in the time-domain (called the intermediate scattering function) $S(\mathbf{Q}, t)$ as

$$S(\mathbf{Q}, \omega) = \int S(\mathbf{Q}, t) e^{-i\omega t} dt, \quad (7.12)$$

where by reference to Eq. (7.11), it is clear that for phonon scattering

$$S(\mathbf{Q}, t) = \frac{1}{N\langle b \rangle^2} \sum_{v, \mu} b_v b_\mu \left\langle \left\langle e^{i\mathbf{Q} \cdot (\mathbf{R}_v(0) - \mathbf{R}_\mu(t))} \right\rangle \right\rangle. \quad (7.13)$$

We now express the atomic position \mathbf{R}_v in terms of the time-average and time-dependent deviation:

$$\mathbf{R}_v(t) = \langle\langle \mathbf{R}_v \rangle\rangle + \mathbf{u}_v(t). \quad (7.14)$$

The intermediate scattering function (Eq. 7.13) can then be expressed as

$$S(\mathbf{Q}, t) = \frac{1}{N\langle b \rangle^2} \sum_{v, \mu} b_v b_\mu e^{i\mathbf{Q} \cdot (\langle\langle \mathbf{R}_v \rangle\rangle - \langle\langle \mathbf{R}_\mu \rangle\rangle)} \left\langle \left\langle e^{i\mathbf{Q} \cdot (\mathbf{u}_v(0) - \mathbf{u}_\mu(t))} \right\rangle \right\rangle \quad (7.15)$$

and expanding the exponential in the time average we get

$$S(\mathbf{Q}, t) = \frac{1}{N\langle b \rangle^2} \sum_{v, \mu} b_v b_\mu e^{i\mathbf{Q} \cdot (\langle\langle \mathbf{R}_v \rangle\rangle - \langle\langle \mathbf{R}_\mu \rangle\rangle)} \left\{ \frac{1 + i\mathbf{Q} \cdot \langle\langle \mathbf{u}_v(0) - \mathbf{u}_\mu(t) \rangle\rangle}{2} - \frac{1}{2} \left\langle \left\langle (\mathbf{Q} \cdot [\mathbf{u}_v(0) - \mathbf{u}_\mu(t)])^2 \right\rangle \right\rangle + \dots \right\}. \quad (7.16)$$

The linear term (the second term within the curly bracket) disappears by thermal averaging. If we denote the remaining first term by $S_0(\mathbf{Q}, t)$ and third term by $S_1(\mathbf{Q}, t)$, we can write Eq. (7.16) as $S(\mathbf{Q}, t) = S_0(\mathbf{Q}, t) + S_1(\mathbf{Q}, t) + \dots$. Substituting back into Eq. (7.12), we get

$$S(\mathbf{Q}, \omega) = S_0(\mathbf{Q}, \omega) + S_1(\mathbf{Q}, \omega) + \dots \quad (7.17)$$

with

$$\begin{aligned} S_0(\mathbf{Q}, \omega) &= \frac{1}{N\langle b \rangle^2} \sum_{v, \mu} b_v b_\mu e^{i\mathbf{Q} \cdot (\langle\langle \mathbf{R}_v \rangle\rangle - \langle\langle \mathbf{R}_\mu \rangle\rangle)} \int e^{-i\omega t} dt \\ &= \frac{1}{N\langle b \rangle^2} \sum_{v, \mu} b_v b_\mu e^{i\mathbf{Q} \cdot (\langle\langle \mathbf{R}_v \rangle\rangle - \langle\langle \mathbf{R}_\mu \rangle\rangle)} \delta(\omega), \end{aligned} \quad (7.18)$$

where $\delta(\omega)$ is the usual Dirac delta function. Thus, S_0 is everywhere zero except when $\omega=0$, $S_0(\mathbf{Q},\omega)=S_0(\mathbf{Q},0)$, and this first term in the expansion contains only elastic scattering.

Now we consider $S_1(\mathbf{Q},\omega)$ which after factoring the square can be written as

$$S_1(\mathbf{Q},\omega) = \frac{1}{2N\langle b \rangle^2} \sum_{v,\mu} b_v b_\mu e^{i\mathbf{Q} \cdot (\langle \mathbf{R}_v \rangle - \langle \mathbf{R}_\mu \rangle)} \\ \times \int \left[\langle \langle (\mathbf{Q} \cdot \mathbf{u}_v(0))^2 \rangle \rangle + \langle \langle (\mathbf{Q} \cdot \mathbf{u}_\mu(t))^2 \rangle \rangle - 2 \langle \langle (\mathbf{Q} \cdot \mathbf{u}_v(0)) (\mathbf{Q} \cdot \mathbf{u}_\mu(t)) \rangle \rangle \right] e^{-i\omega t} dt. \quad (7.19)$$

The first term in the integral is independent of time and can come out of the integral. The second term is also independent of t after thermal averaging (it is equal to the first term) and can also come out of the integral. Thus, as for the case of $S_0(\mathbf{Q},\omega)$, these terms contribute intensity only to the elastic scattering. In fact, they form part of the Debye–Waller factor (Eq. 2.18). Thus, only the third term represents the inelastic intensity. Let us now use the phonon coordinates,

$$\mathbf{u}_v(t) = \frac{1}{\sqrt{N}} \sum_{\mathbf{q}} e^{i(\mathbf{q} \cdot \langle \mathbf{R}_v \rangle - \omega_{\mathbf{q}} t)} \mathbf{u}_{\mathbf{q}}^v(\omega), \quad (7.20)$$

where \mathbf{q} is the phonon wavevector, $\omega_{\mathbf{q}}$ is the frequency of the \mathbf{q} phonon, and $\mathbf{u}_{\mathbf{q}}^v(\omega)$ is its amplitude at the v th atom. If there is more than one atom in the unit cell, $\mathbf{u}_{\mathbf{q}}^v(\omega)$ depends upon v . If we define $G_{v\mu}(\omega) = 2 \int \langle \langle (\mathbf{Q} \cdot \mathbf{u}_v(0)) (\mathbf{Q} \cdot \mathbf{u}_\mu(t)) \rangle \rangle e^{-i\omega t} dt$ and substitute Eq. (7.20) we see that,

$$G_{v\mu}(\omega) = \frac{2}{N} \sum_{\mathbf{q}, \mathbf{q}'} \int e^{i[\mathbf{q} \cdot \langle \mathbf{R}_v \rangle - \mathbf{q}' \cdot \langle \mathbf{R}_\mu \rangle]} \langle \langle (\mathbf{Q} \cdot \mathbf{u}_{\mathbf{q}}^v) (\mathbf{Q} \cdot \mathbf{u}_{\mathbf{q}'}^\mu) e^{-i(\omega_{\mathbf{q}'} - \omega_{\mathbf{q}})t} \rangle \rangle e^{-i\omega t} dt \\ = \frac{2}{N} \sum_{\mathbf{q}} \delta(\omega - \omega_{\mathbf{q}}) e^{i\mathbf{q} \cdot [\langle \mathbf{R}_v \rangle - \langle \mathbf{R}_\mu \rangle]} \langle \langle (\mathbf{Q} \cdot \mathbf{u}_{\mathbf{q}}^v) (\mathbf{Q} \cdot \mathbf{u}_{\mathbf{q}}^\mu) \rangle \rangle. \quad (7.21)$$

By the lattice sum as in Eq. (2.10),

$$S_1(\mathbf{Q},\omega) = \frac{e^{-W}}{\langle b \rangle^2 N} \sum_{\mathbf{q}} \delta(\omega - \omega_{\mathbf{q}}) \delta(\mathbf{Q} + \mathbf{q} - \mathbf{K}) H(\mathbf{Q}, \mathbf{q}), \quad (7.22)$$

where

$$H(\mathbf{Q}, \mathbf{q}) = \sum_{n,m} b_n b_m e^{i(\mathbf{Q} + \mathbf{q}) \cdot (\langle \mathbf{R}_n \rangle - \langle \mathbf{R}_m \rangle)} \langle \langle (\mathbf{Q} \cdot \mathbf{u}_{\mathbf{q}}^n) (\mathbf{Q} \cdot \mathbf{u}_{\mathbf{q}}^m) \rangle \rangle. \quad (7.23)$$

Here e^{-W} is the Debye–Waller factor that comes from the higher-order terms and the sum over n and m is now over atoms in the unit cell and not all atoms in the sample. With the phonon operators,

$$\mathbf{u}_{\mathbf{q},\alpha}^n = \mathbf{e}_{\mathbf{q},\alpha}^n \frac{\hbar}{\sqrt{M\omega_{\mathbf{q},\alpha}}} \left(a_{\mathbf{q},\alpha} + a_{\mathbf{q},\alpha}^\dagger \right), \quad (7.24)$$

where α denotes the phonon branch, $\mathbf{e}_{\mathbf{q},\alpha}^n$ is the polarization unit vector, M is the atomic mass, and $a_{\mathbf{q}}$ and $a_{\mathbf{q}}^\dagger$ are phonon annihilation and creation operators, Eq. (7.23) becomes,

$$H(\mathbf{Q}, \mathbf{q}) = \frac{\hbar^2 Q^2}{2\omega_{\mathbf{q}}} \sum_{n,m,\alpha} \frac{b_n b_m}{\sqrt{M_n M_m}} e^{i(\mathbf{Q}+\mathbf{q}) \cdot (\langle \mathbf{R}_n \rangle - \langle \mathbf{R}_m \rangle)} \left(\hat{\mathbf{Q}} \cdot \mathbf{e}_{\mathbf{q},\alpha}^n \right) \left(\hat{\mathbf{Q}} \cdot \mathbf{e}_{\mathbf{q},\alpha}^m \right) (n_{\mathbf{q},\alpha} + 1), \quad (7.25)$$

where $Q = |\mathbf{Q}|$ and $\hat{\mathbf{Q}} = \mathbf{Q}/Q$. The phonon density is given by the Bose–Einstein factor,

$$n_{\mathbf{q},\alpha} = \frac{1}{e^{\hbar\omega_{\mathbf{q},\alpha}/k_B T} - 1}, \quad (7.26)$$

where k_B is the Boltzmann constant. Equations (7.25) and (7.26) describe the intensity of neutrons or X-rays inelastically scattered by creating single phonons on the energy loss side. The delta function $\delta(\omega - \omega_{\mathbf{q}})$ results in intensity from a given phonon mode appearing only at the energy transfer of the phonon mode frequency (times \hbar). The delta function $\delta(\mathbf{Q} + \mathbf{q} - \mathbf{K})$ results in intensity from that mode appearing at a momentum transfer of $\mathbf{K} - \mathbf{q}$, that is, a distance \mathbf{q} away from a reciprocal lattice (or Bragg) point. A contour plot of $S(\mathbf{Q}, \omega)$ will thus exactly reproduce the phonon dispersion curves with the scattered intensity in each mode given by $e^{-W}/(\langle b \rangle^2 N) H(\mathbf{Q}, \mathbf{q})$. An example of an energy scan of the inelastic scattering intensity is shown in Fig. 7.5. Features resembling the phonon dispersion curves (indeed they are the phonon dispersion curves!) are clearly apparent. Actually, what is plotted in Fig. 7.5b is $S(\mathbf{Q}, \omega)$ and not $S_1(\mathbf{Q}, \omega)$. The single-phonon dispersion curves are evident because of the happy consequence that the multi-phonon terms in the expansion of Eqs. (7.16) and (7.17) just contribute a rather featureless background intensity that $S_1(\mathbf{Q}, \omega)$ sits on top of, as we discuss below.

If the dynamic structure factor is measured with a powder sample, at large Q , the spherical averaging over Q is essentially equivalent to sampling every point in the Brillouin zone. Thus, Eq. (7.25) yields the neutron-weighted density of states. To ensure the accuracy and improve statistics, the data are usually integrated over a range of Q values. An example of the phonon density of states thus determined is shown in Fig. 7.6.

7.2.2. Multi-Phonon Process

We now go back to Eq. (7.16) and consider the effect of the higher-order terms. When Q is small, we only need to consider the leading term in the Q expansion, $S_1(\mathbf{Q}, \omega)$, which is the single-phonon term as seen in Eqs. (7.22) and (7.25). In the

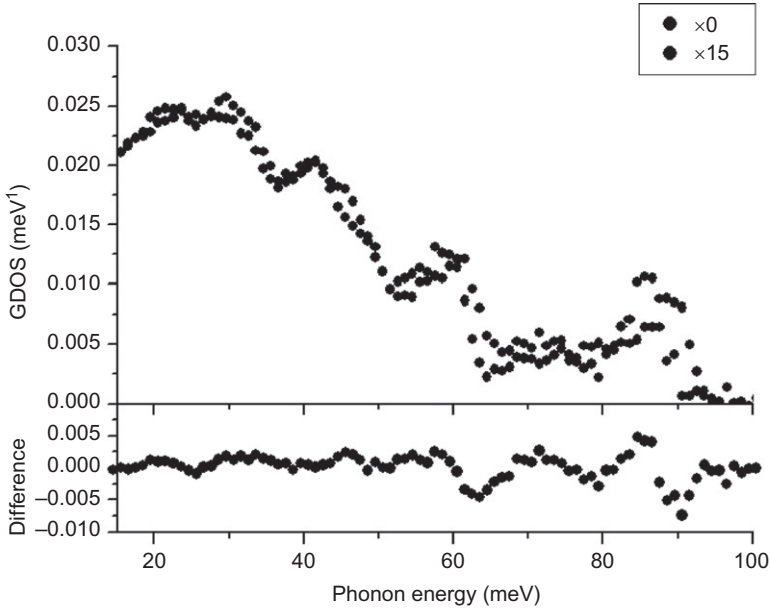


FIGURE 7.6 Phonon density of states of $\text{La}_{2-x}\text{Sr}_x\text{CuO}_4$ ($x=0, 0.15$) determined by inelastic neutron scattering from LRMECS of the IPNS (McQueeney, 2002).

PDF analysis, we cover a wide range of Q values. Thus, it is important to have some idea of the higher-order terms describing the multi-phonon processes. This has been discussed in some detail by Thorpe *et al.* (2002) where the second- and third-order terms have been calculated explicitly for the case of fcc nickel, and powder averaged. These are shown in Fig. 7.7 where it is evident that only the first-order phonon terms have significant structure. However, note that higher-order terms in the phonon spectrum contribute enough information to make them significant if PDF data are used to study lattice dynamics (Reichardt and Pintschovius, 2001; Thorpe *et al.*, 2002).

While it is difficult in general to account fully for the multiple-phonon process, we can safely use an approximate expression, as the multiple sum makes the Q dependence weak and featureless. For this purpose, we note the similarity of the expansions Eqs. (7.16) and (2.16). They are essentially the same expansion, except that Eq. (7.16) is time dependent, while Eq. (2.16) is time averaged. The next term in Eq. (7.16) is proportional to Q^4 and involves two-phonon scattering process. Thus, if we integrate each term over energy, the expansion Eq. (7.16) strongly resembles Eq. (2.16). For large values of Q , the prefactor in Eq. (7.16), which is the structure factor, approaches unity. Thus, the total energy-integrated inelastic scattering intensity is approximated by,

$$S_{\text{inel}}(Q) = \langle \langle (Q \cdot u)^2 \rangle \rangle - \frac{1}{2} \langle \langle (Q \cdot u)^4 \rangle \rangle + \dots \approx 1 - e^{-\langle \langle (Q \cdot u)^2 \rangle \rangle}, \quad (7.27)$$

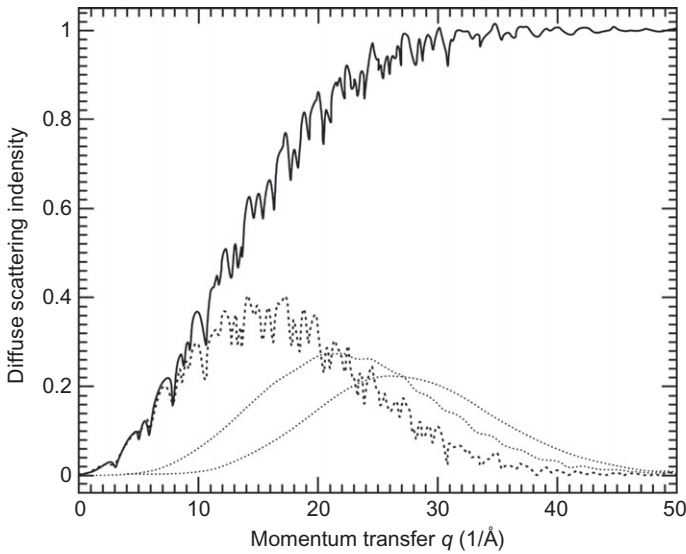


FIGURE 7.7 First- (dotted), second- (dot-dashed), and third- (dot-dot-dashed) order phonon terms calculated explicitly for fcc nickel as it would appear in an ideal total scattering powder diffraction measurement. The solid line is the total phonon scattering (Thorpe *et al.*, 2002).

where the Q^2 terms describe the single-phonon process, Q^4 the two-phonon process, etc. The contribution of each term is shown in Fig. 7.7. The one-phonon part is highly structured but the higher-order terms have very little structure. This result justifies the expression (2.18).

Now at high enough values of Q , the dynamic correlation among atoms is lost, and the scattering of a high-energy probe is described by a ballistic process in which the energy and momentum of the probe is transferred to a single atom. For neutrons, this means the energy loss of

$$\hbar\omega = \frac{\hbar^2 Q^2}{2M}, \quad (7.28)$$

where M is the mass of the atom.

7.3. CORRELATED DYNAMICS AND THE PDF

The phonons in materials give rise to correlations in the dynamics of atoms in real space. This can be intuitively understood in the following way. The simplest model of a solid where the atoms are not interacting is the Einstein model. In this case, every atom oscillates independently around its lattice site with a frequency ω_E . The atomic distribution functions are all Gaussians of the same width, and the pair distribution functions (of pairs of atoms) will just be given by broad Gaussians of width coming from the widths of the atomic

probability distributions added in quadrature. The PDF will consist of a series of peaks at different values of r of equal width, as shown in Fig. 7.8b. The simplest solid where the atoms are strongly interacting is a rigid-body solid where the atoms are rigidly joined (think of a solid metal rod joining them). In this case, motions of the atoms are completely correlated and pairs of atoms are always separated by a fixed distance (the length of the metal rod). In this case, peaks in the PDF will all be delta functions (Fig. 7.8a). A more realistic situation is introduced, when the atoms are joined to each other by stiff springs. In this case, the usual treatment is to transform the problem into normal coordinates (the phonons modes), which are orthogonal and noninteracting, then project the phonon modes back into real space to see what happens there, as we did in Section 7.2. This is mathematically more tractable but is not very intuitive. To understand intuitively what this does to the PDF, consider our rigid-body solid again, but this time cut the metal bar between each pair of atoms and insert a short piece of pliable rubber, the intuitive equivalent of placing a stiff spring there. Now we see that near-neighbor pairs will tend to move in-phase as they did in the rigid-body solid. The pair distribution will be sharp but not a delta function because of the presence of the soft rubber. The second neighbor pair distribution will also be fairly sharp but less so than the near-neighbor distribution because now we have the compliance of two

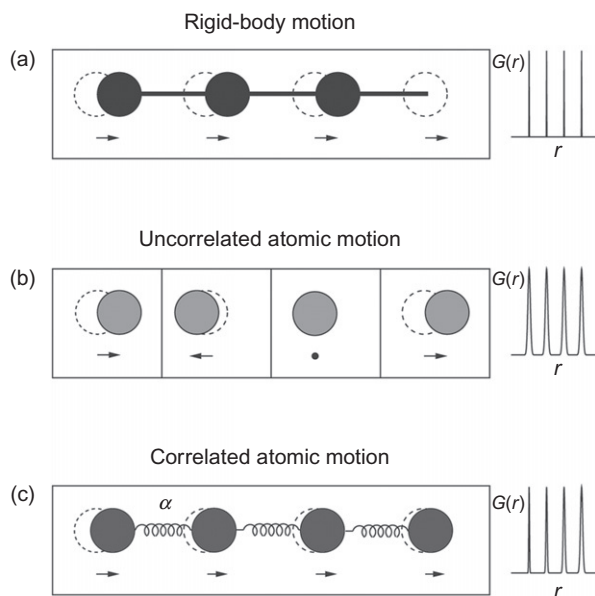


FIGURE 7.8 Schematic of correlated atomic motions showing the resulting PDF peaks on the right. (a) Perfectly correlated motion results in delta function PDF peaks, (b) uncorrelated motion in broad Gaussians, and (c) partially correlated motion in sharp peaks at low- r that broaden with increasing r (Jeong *et al.*, 2003).

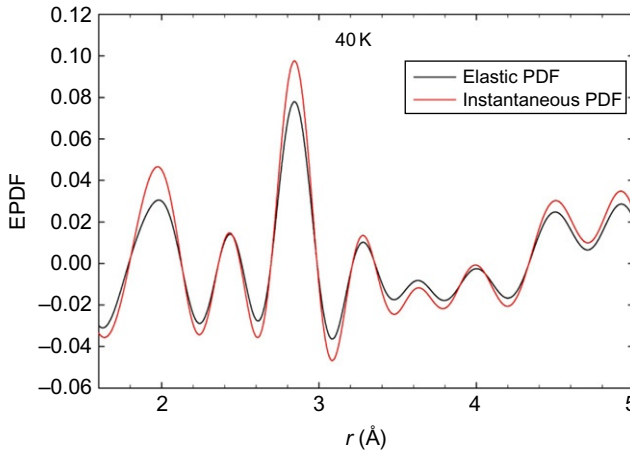


FIGURE 7.9 Elastic and instantaneous PDFs of PMN.

pieces of rubber. The third neighbor motions will be less correlated still because of the third piece of rubber, and so on. Thus, we see that the presence of atomic interactions resulting in phonons introduces an r -dependence to the PDF peak-width. At high pair separations, the motions of the atom pairs converge to the value appropriate for uncorrelated motion. This is shown in Fig. 7.8 (Jeong *et al.*, 2003) with the r -dependence of the peak-widths of the PDF peaks from nickel and InAs shown in Fig. 6.3. The peaks broaden with increasing r and saturate at the uncorrelated motion value. The amplitude of uncorrelated atomic motions is the information contained in the Debye–Waller factor. The additional information in the one-phonon scattering gives rise to the r -dependent PDF peak-widths. In principle, by fitting this r -dependence, we can extract information from the PDF about the atomic potential and the phonons. This is actually no different (other than practical considerations discussed below) than fitting the thermal diffuse scattering from powder diffraction data directly in Q -space, which was first attempted by Warren (1990) as early as 1952, albeit in the PDF case over a much wider range of Q -space.

7.4. DYNAMIC PAIR-DENSITY FUNCTION

Let us now go back to Eq. (7.11) and consider how to represent the lattice dynamics in real space. We assume that the dynamic structure factor, Eq. (7.11), was measured for a powder and show how the local lattice dynamics can be described by applying Fourier-transformation to bring it to real space. First, let us focus on the typical X-ray diffraction measurement with the energy resolution of 1–10 eV. Because the magnitude of energy resolution

is much smaller than the phonon energies (typically less than 0.1 eV), what we obtain by the diffraction measurement is the dynamic structure factor integrated over the energy,

$$S(\mathbf{Q}) = \int_{-\infty}^{\infty} S(\mathbf{Q}, \omega) d\omega = \frac{1}{N \langle b \rangle^2} \sum_{v, \mu} b_v b_\mu \left\langle \left\langle e^{i\mathbf{Q} \cdot (\mathbf{R}_v(0) - \mathbf{R}_\mu(0))} \right\rangle \right\rangle, \quad (7.29)$$

which represents the instantaneous “snapshot,” or the same-time correlation. The Fourier-transform of $S(\mathbf{Q})$ gives the same-time PDF. Intuitively, it is like taking a series of photographs of the moving atoms where the shutter speed of the camera is very fast compared to the atom motions. The duration of the measurement on the other hand is very long, often minutes or hours, and so the resulting data are the superposition of all the snapshots, which sample every instantaneous configuration of the system with the right probability. Thus, the effects of the motion are present in the data even though the measurements are fast, but any correlation in motion is preserved. For example, if two atoms in a pair always move together, you will only ever see them at that fixed distance apart in this measurement. This is discussed in greater detail in [Section 7.5](#).

On the other hand, through an inelastic neutron scattering measurement, we can obtain the energy-resolved dynamic structure factor, $S(\mathbf{Q}, \omega)$. If we choose only the elastic scattering intensity, $S(\mathbf{Q}, 0)$, then in [Eq. \(7.11\)](#), t can be anything when $\omega = 0$. That means the time-dependent or dynamic correlation between the atoms v and μ is ignored in the elastic scattering intensity:

$$S(\mathbf{Q}, 0) = \frac{1}{N \langle b \rangle^2} \sum_{v, \mu} b_v b_\mu \left\langle \left\langle e^{i\mathbf{Q} \cdot \mathbf{R}_v} \right\rangle \right\rangle \left\langle \left\langle e^{-i\mathbf{Q} \cdot \mathbf{R}_\mu} \right\rangle \right\rangle. \quad (7.30)$$

Using the Debye–Waller factor,

$$S(\mathbf{Q}, 0) = \frac{1}{N \langle b \rangle^2} \sum_{v, \mu} b_v b_\mu e^{-\frac{1}{2}(W_v + W_\mu)} e^{i\mathbf{Q} \cdot (\langle \mathbf{R}_v \rangle - \langle \mathbf{R}_\mu \rangle)}. \quad (7.31)$$

Thus, the Fourier-transform of $S(\mathbf{Q}, 0)$ gives the atomic correlation among the time-averaged atomic density function, or the spatial autocorrelation of the time-averaged atomic density, just as the Patterson function. This is different from the “snapshot” picture in [Eq. \(7.29\)](#). The snapshot PDF obtained by Fourier-transforming [Eq. \(7.29\)](#) and the time-averaged PDF obtained by Fourier-transforming [Eq. \(7.30\)](#) are compared in [Fig. 7.9](#). In the Einstein model, these two are the same. But in reality, they differ because phonons are highly correlated collective atomic excitations as discussed in more detail later.

Let us now come back to the dynamic structure factor [Eq. \(7.11\)](#) and see if it can be represented in different ways. Long ago, [van Hove \(1954\)](#) pointed out that the double Fourier-transform of [Eq. \(7.11\)](#) is a real space correlation function,

$$\begin{aligned}\rho(\mathbf{r}, t) &= \int S(\mathbf{Q}, \omega) e^{-i[\mathbf{Q} \cdot \mathbf{r} - \omega t]} d\mathbf{Q} d\omega \\ &= \frac{1}{N \langle b \rangle^2} \sum_{\nu, \mu} b_\nu b_\mu \langle \langle \delta(r - [\mathbf{R}_\nu(0) - \mathbf{R}_\mu(t)]) \rangle \rangle, \end{aligned} \quad (7.32)$$

which is now called the van Hove function. However, this function is rarely used in the analysis of the inelastic scattering data. On the other hand, the $\omega \rightarrow t$ transform of Eq. (7.11),

$$S(\mathbf{Q}, t) = \frac{1}{N \langle b \rangle^2} \sum_{\nu, \mu} b_\nu b_\mu \langle \langle e^{i\mathbf{Q} \cdot (\mathbf{R}_\nu(0) - \mathbf{R}_\mu(t))} \rangle \rangle \quad (7.33)$$

is called the intermediate function (Lovesey, 1984). This function is used regularly in the analysis of neutron scattering data, particularly for overdamped dynamics in liquids and glasses (e.g., Mezei *et al.*, 1987). If the dynamics is not overdamped, however, both Eqs. (7.32) and (7.33) are oscillating functions of time, with all the frequency components mixed up. The dynamic pair-density function (DPDF),

$$\begin{aligned}\rho_0 g(\mathbf{r}, \omega) &= \int S(\mathbf{Q}, \omega) e^{i\mathbf{Q} \cdot \mathbf{r}} d\mathbf{Q} \\ &= \frac{1}{N \langle b \rangle^2} \sum_{\nu, \mu} b_\nu b_\mu \left\langle \left\langle \int \delta(r - [\mathbf{R}_\nu(0) - \mathbf{R}_\mu(t)]) e^{i\omega t} dt \right\rangle \right\rangle \end{aligned} \quad (7.34)$$

was proposed for the purpose of preserving the spectroscopic nature of Eq. (7.11) and yet representing the dynamics in real space (Dmowski *et al.*, 2008). The DPDF describes the pair density of atoms oscillating at a frequency ω and a distance r . Examples of the DPDF, measured and simulated for polycrystalline Ni, are shown in Fig. 7.10. Note that the nearest neighbor peak at 2.5 Å is not split up to about 25 meV (~ 6 THz), but split into two over the frequency range of 25–40 meV (6–10 THz). This is related to the presence of the van Hove singularity in the phonon dispersion of Ni at 32 meV (Birgeneau *et al.*, 1964). Near the van Hove point, the phonon dispersion is flat and becomes easily localized. These localized phonons are recorded clearly in the DPDF, whereas fast dispersing phonons are not. In other words, the DPDF technique is effective in capturing local phonons, but not effective in describing regular phonons. McQueeney (1998) analyzed the DPDF in terms of the phonon coordinates. The results are complex, and no experiment was performed at that time. But the formalism developed in this work is useful for the analysis of the DPDF.

The power of the DPDF technique was clearly demonstrated in the study of relaxor ferroelectric $\text{Pb}(\text{Mg}_{1/3}\text{Nb}_{2/3})\text{O}_3$ (PMN) (Dmowski *et al.*, 2008). Relaxor ferroelectrics are strongly disordered ferroelectrics in which the ferroelectric transition is smeared into a continuous glassy freezing of ferroelectric dynamics. In PMN, Mg^{2+} and Nb^{5+} ions randomly occupy the equivalent crystallographic sites, giving rise to strong disorder in the local electric

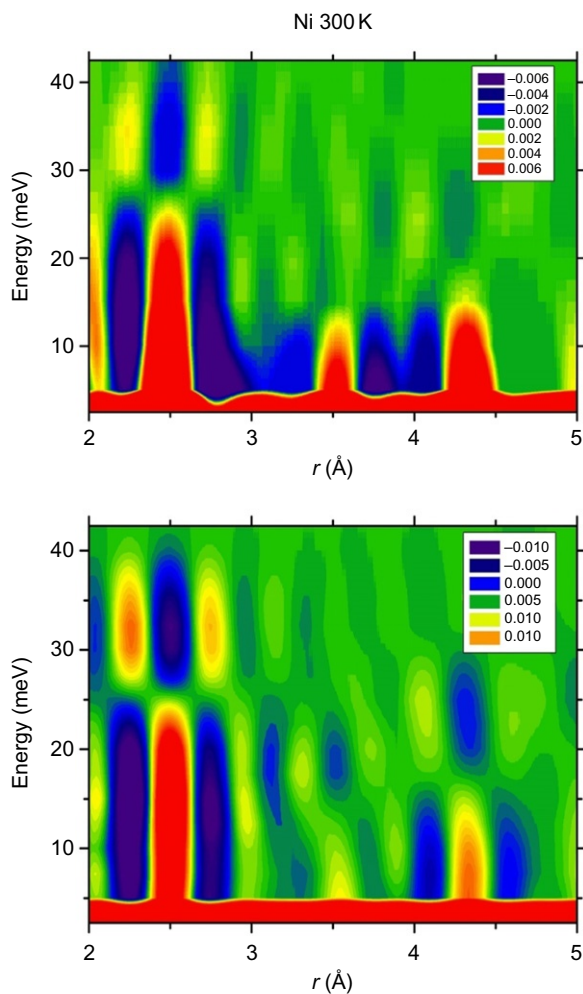


FIGURE 7.10 The DPDF of polycrystalline nickel at 300 K, measured (above) and simulated (below). Colors indicate the intensity of the DPDF as illustrated in the inset. Note that only the local phonons near the van Hove singularity around 32 meV are registered in the DPDF, whereas running phonons with fast dispersion are not detected ([Dmowski *et al.*, 2008](#)).

field gradient. Much of the dielectric polarization is carried by Pb^{2+} ions which are off-centered in the O_{12} cage. In the PDF, Pb off-centering is seen as extra peaks at 2.45 and 3.2 Å ([Egami *et al.*, 1991](#)). Whereas static dielectric polarization disappears above room temperature, dielectric permittivity remains very high over a wide range of temperature, suggesting the system is still dielectrically active. Infrared measurements suggest that dynamic

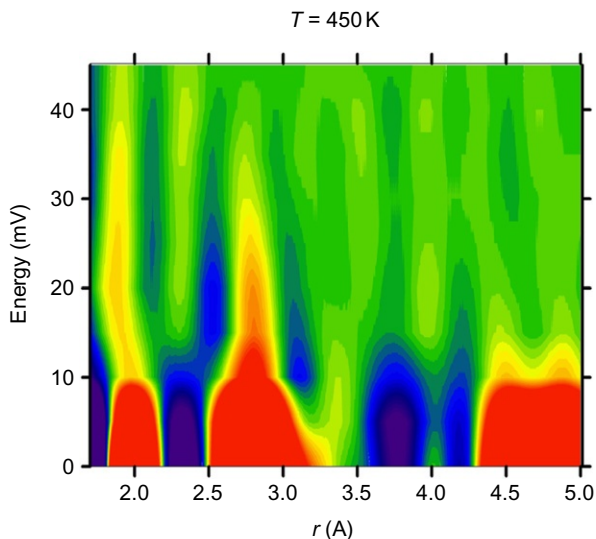


FIGURE 7.11 The DPDF of PMN at 450 K. Note the peak at 2.4 Å is seen only at frequencies greater than 15 meV (Dmowski *et al.*, 2008).

polarizations remain up to 600 K, now called the Burns temperature (Burns and Scott, 1973).

The DPDF of PMN determined at 450 K reveals what is going on. As shown in Fig. 7.11, where the DPDF intensity is color coded, the peak at 2.4 Å is not seen in the static structure at $\omega=0$, but is seen at frequencies higher than 15 meV ($\sim 4 \text{ THz}$). So at 450 K, Pb is dynamically polarized with frequencies larger than 4 THz. Figures 7.12 and 7.13 show the evolution with temperature. The static PDF ($\omega=0$) shown in Fig. 7.12 suggests static polarization indeed disappears around room temperature. But dynamic polarization at 15 meV, shown in Fig. 7.13, persists up to 600 K, as suggested by the IR measurements. Thus, the DPDF directly demonstrated the presence of dynamic polarization up to the Burns temperature.

The example of PMN clearly illustrates the power of the DPDF method to describe local dynamics. This method is currently used in the study of liquid dynamics and providing us with unique information not available hitherto.

7.5. EFFECT OF INELASTIC SCATTERING ON THE PDF

7.5.1. Placzek Correction

We now consider the regular powder diffraction measurement and how the local lattice dynamics would affect the PDF. Let us first look at the X-ray scattering. It is often claimed that “since the x-rays are so fast that x-ray

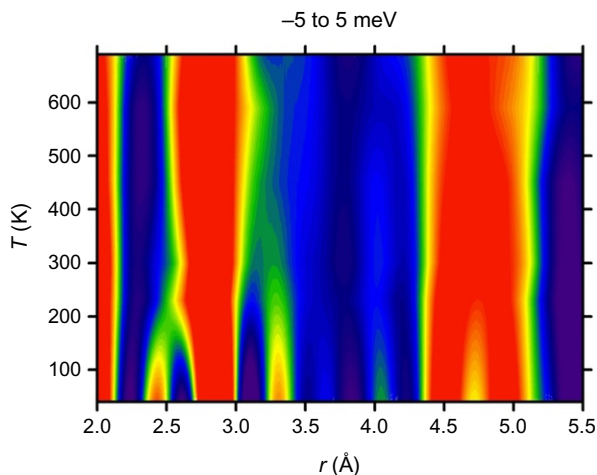


FIGURE 7.12 Temperature dependence of the DPDF at $\omega=0$ (integrated ω from -5 to 5 meV) that describes the static structure. Static polarization indicated by the extra peaks at 2.4 and 3.3 Å disappears above room temperature (Dmowski *et al.*, 2008).

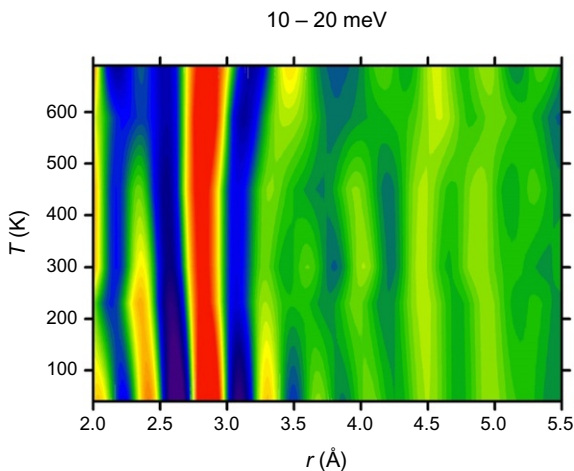


FIGURE 7.13 Temperature dependence of the DPDF at $\omega=15$ meV (integrated ω from 10 to 20 meV). Dynamic polarization indicated by the extra peaks at 2.4 and 3.3 Å persists up to 600 K (Dmowski *et al.*, 2008).

diffraction is a snap-shot of the structure” (e.g., Warren, 1990). While this statement is not altogether wrong, it is slightly misleading. As we mentioned earlier, X-ray inelastic scattering measurements are now becoming a reality, and even the lattice dynamics can be studied by X-ray scattering. We show at first that the “speed” of the measurement is determined primarily by the

energy resolution of the spectrometer. The *velocity* of the probe is relevant only in setting up the effective energy resolution when an energy analyzer is not used in the diffractometer. We then introduce the Placzek correction for neutron scattering.

In the inelastic scattering measurement, both Q and ω are determined with the energy resolution, typically of the order of 1 meV or better for both neutron scattering and X-ray scattering as discussed in [Section 7.1](#). However, in the conventional X-ray powder scattering experiment, the energy resolution is of the order of 1–10 eV, far larger than the phonon energies. Thus, what is measured is the dynamic structure factor integrated over a certain energy range,

$$S_{\text{powder}}(Q) = \int W(\omega) S(Q(\omega), \omega) d\omega, \quad (7.35)$$

where $W(\omega)$ is a resolution (window) function. Therefore, the nominally “elastic” X-ray scattering intensity includes the inelastic scattering contribution due to phonons. Now the velocity of light becomes important here; since the velocity of light is high, the momentum transfer associated with the energy transfer of 10 eV is very small ($\Delta k \sim 10^{-3} \text{ \AA}^{-1}$) compared to the reciprocal lattice vector ($\sim 1 \text{ \AA}^{-1}$). Thus, the magnitudes of \mathbf{k}_{init} and $\mathbf{k}_{\text{final}}$ are very close to each other, and Q is practically independent of ω . If $W(\omega)$ is constant over the relevant range of ω , then the window function is much wider than the phonon band width, from [Eq. \(7.11\)](#),

$$\begin{aligned} S(\mathbf{Q}) &= \frac{1}{N\langle b \rangle^2} \sum_{\nu, \mu} b_{\nu} b_{\mu} \int \int \left\langle \left\langle e^{i\mathbf{Q} \cdot (\mathbf{R}_{\nu}(0) - \mathbf{R}_{\mu}(t))} \right\rangle \right\rangle e^{-i\omega t} dt d\omega \\ &= \frac{1}{N\langle b \rangle^2} \sum_{\nu, \mu} b_{\nu} b_{\mu} \left\langle \left\langle e^{i\mathbf{Q} \cdot (\mathbf{R}_{\nu}(0) - \mathbf{R}_{\mu}(0))} \right\rangle \right\rangle. \end{aligned} \quad (7.36)$$

Thus, $S(\mathbf{Q})$ measures the instantaneous (same-time) correlation [Eq. \(7.29\)](#). This justifies the common declaration that the X-ray diffraction takes the “snapshot” of the atomic configuration. The snapshots, however, are continuously taken and time averaged. In that sense, the “snapshot” is not really an appropriate expression, and students are often confused on this point. It is, therefore, more accurate to call $S(Q)$ the same-time correlation function.

Neutrons, on the other hand, have velocities that are much slower than the speed of light and are even comparable to the velocity of atoms. Thus, for neutron scattering, the magnitudes of \mathbf{k}_{init} and $\mathbf{k}_{\text{final}}$ can be significantly different, and for a fixed scattering angle, Q is dependent upon ω as in [Eq. \(7.7\)](#). This causes a problem for a powder diffraction measurement in which the actual energy and momentum transfers are not measured. In the powder diffraction measurement using a reactor, only the initial energy is defined by a monochromator, whereas the final energy is not measured. In the TOF measurement, only the total time-of-flight is recorded, and neither the initial nor final energies and momenta are actually measured. To circumvent this

problem, what is usually done is to assume the momentum transfer of Q_0 for every scattering process, elastic or inelastic, and make appropriate corrections later. This correction is known as the Placzek correction (Placzek, 1952).

In the Placzek correction, the neutron is assumed to have a high energy and to be scattered by an atom ballistically, which means that the energy lost by a neutron is transferred entirely to the kinetic energy of the atom,

$$\hbar\omega = \frac{\hbar^2}{2M} \left(|\mathbf{q}_{\text{final}}|^2 - |\mathbf{q}_{\text{init}}|^2 \right), \quad (7.37)$$

$$\mathbf{Q} = \mathbf{q}_{\text{init}} - \mathbf{q}_{\text{final}},$$

where \mathbf{q}_{init} and $\mathbf{q}_{\text{final}}$ are the momenta of the atom before and after scattering. In this case, the energy transfer depends only on the atomic mass M , and not on the restoring force represented by the Debye temperature. In spite of such a simplification, the Placzek correction works well most of the time.

The Placzek correction was developed for a triple-axis spectrometer with which the energy of incident neutrons is fixed. By assuming that the energy of the incident neutron is much larger than the energy transfer, from Eq. (7.7) we obtain,

$$\begin{aligned} Q^2 &= 2k_i^2 + \frac{2m\omega}{\hbar} - 2k_i^2 \cos 2\theta \left(1 + \frac{2m\omega}{\hbar k_i^2} \right)^{1/2} \\ &= 2k_i^2 + \frac{2m\omega}{\hbar} - 2k_i^2 \cos 2\theta \left(1 + \frac{m\omega}{\hbar k_i^2} + \dots \right) \\ &= 4k_i^2 \sin^2 \theta \left(1 + \frac{m\omega}{\hbar k_i^2} + \dots \right) \end{aligned} \quad (7.38)$$

and

$$Q = 2k_i \sin \theta \left(1 + \frac{m\omega}{2\hbar k_i^2} + \dots \right). \quad (7.39)$$

If we neglect the initial velocity of the atom, the kinetic energy gain of the atom due to the momentum transfer of Q is,

$$\hbar\omega = \frac{\hbar^2}{2M} Q^2, \quad (7.40)$$

where M is the atomic mass. Thus, we obtain the first-order shift in Q ,

$$\frac{\Delta Q}{Q_0} = \frac{m\omega}{2\hbar k_i^2} = \frac{m}{M} \sin^2 \theta + \dots \quad (7.41)$$

Thus, the Placzek shift becomes important at high scattering angles.

In the case of the TOF measurement, it is more complex because the result depends upon the neutron flight path length from the target to the sample, L_1 , and that from the sample to the detector, L_2 . The time-of-flight, t , is the sum of the flight times over L_1 and L_2 with the velocities v_1 and v_2 , respectively,

$$t = \frac{L_1}{v_1} + \frac{L_2}{v_2} = \frac{mL_1}{\hbar k_{\text{init}}} + \frac{mL_2}{\hbar k_{\text{final}}}. \quad (7.42)$$

Thus, the nominal momentum, k_0 , is given by,

$$k_0 = \frac{mL}{\hbar t} = \frac{1}{\frac{L_1}{Lk_{\text{init}}} + \frac{L_2}{Lk_{\text{final}}}}, \quad (7.43)$$

where $L = L_1 + L_2$. The nominal momentum transfer, Q_0 , calculated assuming elastic scattering, is given by

$$Q_0 = 2k_0 \sin \theta = \frac{2 \sin \theta}{\frac{L_1}{Lk_{\text{init}}} + \frac{L_2}{Lk_{\text{final}}}}. \quad (7.44)$$

Combining Eq. (7.44) with Eqs. (7.4) and (7.5), the relationship between the nominal momentum transfer and the real momentum transfer is obtained. Since usually $L_1 \gg L_2$ for most spectrometers, Eq. (7.44) can be expanded into,

$$Q_0 = \frac{2k_{\text{init}} \sin \theta}{1 + \frac{L_2}{L} \left(\frac{k_{\text{init}}}{k_{\text{final}}} - 1 \right)}. \quad (7.45)$$

If we further assume $\hbar\omega \ll \hbar^2 k^2 / 2m$, then,

$$Q_0 = \frac{2k_{\text{init}} \sin \theta}{1 - \frac{L_2}{L} \frac{m\omega}{\hbar k_{\text{init}}^2}} = 2k_{\text{init}} \sin \theta \left(1 + \frac{L_2}{L} \frac{m\omega}{\hbar k_{\text{init}}^2} + \dots \right). \quad (7.46)$$

From Eq. (7.39),

$$Q = Q_0 \left(1 - \left(1 - \frac{2L_2}{L} \right) \delta + \dots \right), \quad (7.47)$$

$$\delta = \frac{m\omega}{2\hbar k_{\text{init}}^2}.$$

The main effect of the Placzek correction for the TOF measurement is to correct the spectrum of the incident energies, since the normalization is usually done assuming elastic scattering alone. Incidentally, from Eq. (7.47), it is obvious that the first-order Placzek correction vanishes if $L_2 = L/2$ or $L_1 = L_2$. However, the price to pay is the large size of the detector housing and the large angle the spectrometer takes up around the source. In terms of financial cost and real estate, it is an expensive proposition.

However, the Placzek correction is valid only at high Q , high-energy ranges where the ballistic approximation is justified. In reality, it seriously

overcorrects the inelastic effect. This is because at low Q , up to 10 \AA^{-1} or more, much of the scattering is *elastic*, as in Eq. (7.18). For this reason, we recommend to *turn off the Placzek correction for the PDF analysis*. The standard PDF analysis programs such as the GUI program PDFgetN has an option for turning off the Placzek correction. An alternative is to evaluate Eq. (7.17) using the phonon model, such as the Einstein or Debye models, and actually calculate the inelastic contributions. Such an effort is under way.

7.5.2. Effective Energy Window for the Neutron PDF Method

For X-ray powder diffraction, the ω dependence of Q is negligible, so we obtain the same-time correlation function as we discussed above. For neutron powder diffraction, the situation is more complex, because we cannot neglect the ω dependence of Q . For large ω , the Placzek shift is so large that the integration over ω mixes up signals, and Eq. (7.35) becomes incoherent and the information gets lost. Thus, the Placzek shift imposes an effective energy window.

It is not easy to evaluate how wide the effective window is. It should vary from one spectrometer to the other because of the difference in the L_1 to L_2 ratio. We have at least one case where estimation can be made, because the same sample was studied by both the regular PDF and the DPDF. The temperature evolution of the local dynamics in PMN was studied both by the PDF using the NPDF spectrometer at the Lujan Center of the Los Alamos National Laboratory (Jeong *et al.*, 2005) and by the DPDF using the PHAROS, also at the Lujan Center (Dmowski *et al.*, 2008).

By comparing the PDF and DPDF of PMN, it becomes clear that the PDF is dominated by the static component which disappears around 300 K. The dynamic part which persists up to 600 K is recorded only as a weak tail in the PDF. Therefore, the effective window width must be about 5 meV for the NPDF.

7.5.3. Phonon Dispersion and the PDF

As early as 1952, attempts were made to extract phonon dispersions from X-ray powder diffraction data (Warren, 1990). It was quickly realized that the extensive powder averaging made this difficult and attention was switched to fitting thermal diffuse scattering from single crystals (Warren, 1990), and ultimately, with the advent of inelastic neutron scattering, to measure them directly. However, there is still great interest in the possibility of extracting atomic potential parameters and phonon information from powder data in cases where single crystals are not available or where data need to be measured in special environments such as high pressure cells. Powder diffraction has also traditionally had an advantage in phase diagram studies because of the relative ease of measuring and analyzing multiple data sets collected as a function of temperature and composition. In these cases, extracting phonon

information from powder data would facilitate studies of, for example, phonon softening. One of the problems of the early studies was that the powder data were studied over a relatively narrow range of Q -space. Since the phonon intensity, $S_1(\mathbf{Q}, \omega)$, contributes relatively little to the total measured intensity, it is necessary to measure $S(Q)$ over a wide range of Q with very good statistics to make progress. This happens as a fairly natural consequence of taking data to obtain the PDF as we discussed in detail in [Chapter 5](#). Interest has, therefore, recently been reawakened in the possibility of extracting phonon information from PDF-quality data measured at modern sources using modern techniques. Initial claims that force-constant variables could be measured with the same accuracy as possible from INS ([Dimitrov *et al.*, 1999](#)) are controversial ([Jeong *et al.*, 1999](#); [Reichardt and Pintschovius, 2001](#); [Thorpe *et al.*, 2002](#)). Nonetheless, significant information about the atomic potential is present in the PDF ([Jeong *et al.*, 2003](#); [Goodwin *et al.*, 2005](#)), the only question is how many variables can reasonably be extracted and with what accuracy. Work needs to be done to improve the accuracy of determining $S(Q)$, and, at present, it is not clear how much impact this kind of study will have in the future. We also note that with the use of high-energy X-ray diffraction, it is becoming much quicker and easier to measure the thermal diffuse scattering from single crystals directly ([Holt *et al.*, 1999](#)). But at the same time, the advent of IXS with the energy resolution better than 1 meV ([Section 7.1.2](#)) made it easier to measure the phonon dispersion directly even for small single crystals.

7.5.4. Hybrid Techniques

The measurement with a monochromatic incident beam, however, is inefficient, since only a small portion of the incident spectrum is utilized in the incident beam. On the other hand, the regular PDF approach has a sloppy energy resolution, so that the method to determine the lattice dynamics from the PDF is applicable only when the phonon dispersion can be described by a small number of parameters. For some applications, it is useful to consider the hybrid technique between the two. For a powder sample, the dynamic structure factor depends only on the magnitude of Q , not on the direction, thus $S(Q, \omega)$ is the same for all the detectors. For truly elastic scattering, every detector measures the same $S(Q)$, and only the relation between Q and TOF and the range of Q depends on the scattering angle θ . Thus, any deviation in the measured $S(Q)$ among the detectors should originate from dynamic scattering.

In principle, $S(Q, \omega)$ can be determined in such a way that it explains the measured $S(Q)$ for all the detectors. The direct method proposed by [Dimitrov *et al.* \(1999\)](#) should be capable of such determination, if the Placzek correction was incorporated. However, it would require a massive computational effort, and the accuracy of the outcome is difficult to estimate. A simpler compromise is to use a nearly monochromatic incident beam, but with a

relatively wide momentum spectrum, $P(\Delta k_i, k_{i0})$, where k_{i0} is the average momentum and $\Delta k_i = k_i - k_{i0}$. Such a beam can be produced by a chopper with a wide aperture, a sloppy chopper. The use of wide aperture increases the measured intensity. Then the TOF spectrum of scattered neutrons is given by

$$I(t, \theta) = \int P(\Delta k_i, k_{i0}) S(k_i, k_f) d\Delta k_i, \quad (7.48)$$

where $S(Q, \omega)$ is expressed in terms of k_i and k_f . From Eq. (7.44), $k_f = k_{f0} + \Delta k_f$, where

$$\frac{1}{k_{f0}} = \frac{\hbar t}{mL_2} - \frac{L_1}{L_2 k_{i0}}, \quad (7.49)$$

$$\Delta k_f = -\frac{L_1 k_{f0}^2}{L_2 k_{i0}^2} \Delta k_i. \quad (7.50)$$

Now from Eqs. (7.3) and (7.5),

$$\hbar\omega = \hbar\omega_0 + \frac{\hbar^2}{m}(k_{f0}\Delta k_f - k_{i0}\Delta k_i), \quad (7.51)$$

$$Q^2 = Q_0^2 + 2(k_{i0} - k_{f0} \cos 2\theta)\Delta k_i + 2(k_{f0} - k_{i0} \cos 2\theta)\Delta k_f, \quad (7.52)$$

where

$$\hbar\omega_0 = \frac{\hbar^2}{2m}(k_{f0}^2 - k_{i0}^2), \quad (7.53)$$

$$Q_0^2 = k_{f0}^2 + k_{i0}^2 - 2k_{f0}k_{i0} \cos 2\theta. \quad (7.54)$$

Thus, $S(Q, \omega)$ can be expanded in terms of $\Delta Q = Q - Q_0$ and $\Delta\omega = \omega - \omega_0$,

$$\begin{aligned} S(Q, \omega) &= S(Q_0, \omega_0) + \frac{\partial S}{\partial Q} \Delta Q + \frac{\partial S}{\partial \omega} \Delta\omega \\ &+ \frac{1}{2} \left[\frac{\partial^2 S}{\partial Q^2} (\Delta Q)^2 + \frac{\partial^2 S}{\partial \omega^2} (\Delta\omega)^2 \right] + \frac{\partial S}{\partial Q} \frac{\partial S}{\partial \omega} \Delta Q \Delta\omega + \dots \end{aligned} \quad (7.55)$$

where

$$\Delta\omega = \frac{\hbar}{m}(k_{f0}\Delta k_f - k_{i0}\Delta k_i) \quad (7.56)$$

and

$$\Delta Q = \frac{1}{Q_0} [(k_{i0} - k_{f0} \cos 2\theta)\Delta k_i + (k_{f0} - k_{i0} \cos 2\theta)\Delta k_f]. \quad (7.57)$$

Now we define the moments of $P(\Delta k_i, k_{i0})$,

$$\begin{aligned} K_0 &= \int P(\Delta k_i, k_{i0}) d\Delta k_i = 1, \\ K_1 &= \int P(\Delta k_i, k_{i0}) \Delta k_i d\Delta k_i = 0, \\ K_2 &= \int P(\Delta k_i, k_{i0}) (\Delta k_i)^2 d\Delta k_i, \end{aligned} \quad (7.58)$$

where we assumed that $P(\Delta k_i, k_{i0})$ is a symmetric function. Then Eq. (7.48) is given by,

$$I(t, \theta) = S(Q_0, \omega_0) + K_2 (A_0 + A_1 \cos 2\theta + A_2 \cos^2 2\theta), \quad (7.59)$$

where A_0 , A_1 , and A_2 can be determined from Eqs. (7.48)–(7.55). Thus, the dependence of $I(t, \theta)$ on $\cos 2\theta$ and the continuity condition for $S(Q, \omega)$ yield the coefficients dS/dQ , etc. These can be used in refining $S(Q, \omega)$ with the accuracy higher than the initial resolution warranted. In this method, using a forgiving energy resolution increases the count rate and reduces statistical noise, and $S(Q, \omega)$ can be determined with higher accuracy.

A7.1. SIMPLE DERIVATION

In this chapter, we introduced the dynamical structure factor Eq. (7.11),

$$S(\mathbf{Q}, \omega) = \frac{1}{N \langle b \rangle^2} \sum_{\nu, \mu} b_\nu b_\mu \int \left\langle \left\langle e^{i\mathbf{Q} \cdot (\mathbf{R}_\nu(0) - \mathbf{R}_\mu(t))} \right\rangle \right\rangle e^{-i\omega t} dt. \quad (A7.1)$$

As in the case of static structure function (sample scattering amplitude), this equation can be derived by comparing the phases of the incoming and outgoing waves, by explicitly including time dependence. The incoming wave is expressed by,

$$\phi_{k_{\text{init}}}(\mathbf{r}, t) = e^{i(\mathbf{k}_{\text{init}} \cdot \mathbf{r} - \omega_{\text{init}} t)}. \quad (A7.2)$$

The scattered wave is

$$\chi_{k_{\text{final}}}(\mathbf{r}, t) = A e^{i(\mathbf{k}_{\text{final}} \cdot \mathbf{r} - \omega_{\text{final}} t)}. \quad (A7.3)$$

Here the amplitude A is independent of time. Otherwise the scattered wave (Eq. A7.3) would not have the energy of $\hbar\omega_{\text{final}}$. Thus, at the point of scattering by the atom ν at time t' , taking into account that the position of the atom, \mathbf{R}_ν , changes with time, the continuity condition is

$$\begin{aligned} \chi_{k_{\text{final}}}(\mathbf{R}_\nu(t'), t') &= B \phi_{k_{\text{init}}}(\mathbf{R}_\nu(t'), t'), \\ A e^{i(\mathbf{k}_{\text{final}} \cdot \mathbf{R}_\nu(t') - \omega_{\text{final}} t')} &= B e^{i(\mathbf{k}_{\text{init}} \cdot \mathbf{R}_\nu(t') - \omega_{\text{init}} t')}. \end{aligned} \quad (A7.4)$$

Thus,

$$A = B e^{i[(\mathbf{k}_{\text{init}} - \mathbf{k}_{\text{final}}) \cdot \mathbf{R}_\nu(t') - (\omega_{\text{init}} - \omega_{\text{final}}) t']} = B e^{i(\mathbf{Q} \cdot \mathbf{R}_\nu(t') - \omega t')}. \quad (A7.5)$$

Therefore, the scattering amplitude for inelastic scattering at time t' is given by,

$$\Psi(\mathbf{Q}, t') = \frac{1}{\langle b \rangle} \sum_{\mathbf{v}} b_{\mathbf{v}} e^{i(\mathbf{Q} \cdot \mathbf{R}_{\mathbf{v}}(t') - \omega t')}. \quad (\text{A7.6})$$

At the time of observation, t , all the scattering incidents in the past have to be integrated over time t' ,

$$\Psi(\mathbf{Q}, \omega) = \int \Psi(\mathbf{Q}, t') dt' = \frac{1}{\langle b \rangle} \sum_{\mathbf{v}} b_{\mathbf{v}} \int e^{i(\mathbf{Q} \cdot \mathbf{R}_{\mathbf{v}}(t') - \omega t')} dt'. \quad (\text{A7.7})$$

The dynamical structure factor is defined by

$$S(\mathbf{Q}, \omega) = \frac{1}{N} |\Psi(\mathbf{Q}, \omega)|^2. \quad (\text{A7.8})$$

Thus,

$$\begin{aligned} S(\mathbf{Q}, \omega) &= \frac{1}{N} \iint \Psi(\mathbf{Q}, t') \Psi^*(\mathbf{Q}, t'') dt' dt'' \\ &= \frac{1}{N \langle b \rangle^2} \sum_{\mathbf{v}, \mu} b_{\mathbf{v}} b_{\mu} \int \int e^{i(\mathbf{Q} \cdot \mathbf{R}_{\mathbf{v}}(t') - \omega t')} dt' \int e^{-i(\mathbf{Q} \cdot \mathbf{R}_{\mu}(t'') - \omega t'')} dt'' \\ &= \frac{1}{N \langle b \rangle^2} \sum_{\mathbf{v}, \mu} b_{\mathbf{v}} b_{\mu} \int \int e^{i\mathbf{Q} \cdot [\mathbf{R}_{\mathbf{v}}(t') - \mathbf{R}_{\mu}(t'')]} e^{-i\omega(t' - t'')} dt' dt'' \\ &= \frac{1}{N \langle b \rangle^2} \sum_{\mathbf{v}, \mu} b_{\mathbf{v}} b_{\mu} \int \int e^{i\mathbf{Q} \cdot [\mathbf{R}_{\mathbf{v}}(t') - \mathbf{R}_{\mu}(t - t'')]} e^{i\omega t} dt' dt \\ &= \frac{1}{N \langle b \rangle^2} \sum_{\mathbf{v}, \mu} b_{\mathbf{v}} b_{\mu} \int \int \left\langle \left\langle e^{i\mathbf{Q} \cdot [\mathbf{R}_{\mathbf{v}}(0) - \mathbf{R}_{\mu}(t)]} \right\rangle \right\rangle e^{i\omega t} dt. \end{aligned} \quad (\text{A7.9})$$

The last step uses the fact that the time average (over t') is equal to the ensemble (thermal) average.

REFERENCES

- Birgeneau, R.J., Cordes, J., Dolling, G. & Woods, A.D.B. (1964) *Phys. Rev.*, **136**, A1359.
 Burns, G. & Scott, B.A. (1973) *Solid State Commun.*, **13**, 423.
 Dimitrov, D.A., Louca, D. & Röder, H. (1999) *Phys. Rev. B*, **60**, 6204.
 Dmowski, W., Vakhrushev, S.B., Jeong, I.-K., Hehlen, M.P., Trouw, F. & Egami, T. (2008) *Phys. Rev. Lett.*, **100**, 137602.
 Egami, T., Rosenfeld, H.D., Toby, B.H. & Bhalla, A. (1991) *Ferroelectrics*, **120**, 11.
 Egami, T., Chung, J.-H., McQueeney, R.J., Yethiraj, M., Mook, H.A., Frost, C., Petrov, Y., Dogan, F., Inamura, Y., Arai, M., Tajima, S. & Endoh, Y. (2002) *Physica B*, **62**, 316.
 Goodwin, A.L., Tucker, M.G., Cope, E.R., Dove, M.T. & Keen, D.A. (2005) *Phys. Rev. B*, **72**, 214304.

- Holt, M., Wu, Z., Hong, H., Zschack, P., Jemian, P., Tischler, J., Chen, H. & Chiang, T.-C. (1999) *Phys. Rev. Lett.*, **83**, 3317.
- Jeong, I.-K., Proffen, T., Mohiuddin-Jacobs, F. & Billinge, S.J.L. (1999) *J. Phys. Chem. A*, **103**, 921.
- Jeong, I.-K., Heffner, R.H., Graf, M.J. & Billinge, S.J.L. (2003) *Phys. Rev. B*, **67**, 104301.
- Jeong, I.-K., Darling, T.W., Lee, J.K., Proffen, Th, Heffner, R.H., Park, J.S., Hong, K.S., Dmowski, W. & Egami, T. (2005) *Phys. Rev. Lett.*, **94**, 147602.
- Lake, B., Tennant, D.A. & Nagler, S.E. (2000) *Phys. Rev. Lett.*, **85**, 832.
- Lovesey, S.W. (1984) *Theory of Neutron Scattering from Condensed Matter*. Oxford: Oxford Science Publications.
- McQueeney, R.J. (1998) *Phys. Rev. B*, **57**, 10560.
- McQueeney, R.J. (2002) Private communication. See McQueeney, R.J., Sarrao, J.L., Pagliuso, P.G., Stephens, P.W. & Osborn, R. (2001) *Phys. Rev. Lett.* **87**, 077001.
- Mezei, F., Knaak, W. & Farago, B. (1987) *Phys. Rev. Lett.*, **58**, 571.
- Placzek, G. (1952) *Phys. Rev.*, **86**, 377.
- Reichardt, W. & Pintschovius, L. (2001) *Phys. Rev. B*, **63**, 174302.
- Sinn, H., Alp, E.E., Alatas, A., Barraza, J., Bortel, G., Burkel, E., Shu, D., Sturhahn, W., Sutter, J.P., Toellner, T.S. & Zhao, J. (2001) *Nucl. Instrum. Methods Phys. Res. A*, **467**, 1545.
- Thorpe, M.F., Levashov, V.A., Lei, M. & Billinge, S.J.L. (2002) *From Semiconductors to Proteins: Beyond the Average Structure*. New York: Kluwer/Plenum pp. 105.
- Tranquada, J.M., Shirane, G. & Shapiro, S.M. (2002) *Neutron Scattering with a Triple-Axis Spectrometer*. Cambridge: Cambridge University Press.
- van Hove, L. (1954) *Phys. Rev.*, **95**, 249.
- Warren, B.E. (1990) *X-ray Diffraction*. New York: Dover.